Available online at www.sciencedirect.com
SCIENCE DIRECT®

Polymer 46 (2005) 4283–4295

polymer

www.elsevier.com/locate/polymer

Disorder effects on the strain response of model polymer networks

Carsten Svaneborg[a,*], Gary S. Grest[b], Ralf Everaers[a]

[a]*Max-Planck-Institut für komplexer Systeme, Nöthnitzer Street 38, D-01187 Dresden, Germany*
[b]*Sandia National Laboratories, Albuquerque, NM 87185, USA*

Abstract

Molecular dynamics simulations are used to investigate polymer networks made by either end-linking or randomly crosslinking a melt of linear precursor chains. The resulting network structures are very different, since end-linking leads to nearly ideal monodisperse networks, while random crosslinking leads to polydisperse networks, characterized by an exponential strand length distribution. Networks with average strand length 20 and 100 were generated. These networks were used to study the effects of disorder in the network connectivity on observables averaged either over the entire network or selected sub-structures. Heterogeneities in the randomly crosslinked networks cause significant differences in the localization of monomers, however, neither the localization of crosslinks nor the microscopic strain response are significantly affected. Compared to end-linked networks, randomly crosslinked networks have a slightly increased tube diameter, and as a result a slightly decreased shear modulus, but otherwise identical stress–strain behavior. For the investigated systems, we conclude that the microscopic strain response, tube diameter, and stress–strain relation are all insensitive to the heterogeneities due to the linking process by which the network were made.

Keywords: Rubber elasticity theory; Network structure; Computer simulation

1. Introduction

Polymer networks such as vulcanized natural rubber have been studied for more than two centuries [1,2] and remain a very active field of research. Computer simulations play an increasingly important role, since they allow for control over and access to the microscopic network structure and its reponse to deformations [3,4]. Selected examples of very recent progress using computer simulations with emphasis of formation and structure of polymer networks are atomistic molecular dynamics simulations of PDMS network formation [5], reversibly self-assembled tri-functional networks of flexible or semiflexible chains [6], studies of networks formation by non-stoichiometric crosslinking [7,8], effects of non-spherical filler particles [9,10], effects of mixtures of different crosslink functionalties [11], and a topological characterization of network structure of end-linked and randomly crosslinked networks for different strand lengths [12]. Computer simulations also allow the effects of microstructures in the melt state prior to crosslinking to be studied. For example the effects of chain stiffness and volume fraction of precursor chains on network formation and structure [13], networks formed by crosslinking an AB copolymer melt microphase separated into a lamellar phase [14], and networks formed by end-linking a melt consisting of short and long strands [15].

The theoretical description of polymer networks remains a challenge [1,16–20]. Understanding the molecular origin of stress production in polymer networks is not only of fundamental physical interest but also important for the design of systems optimized for practical applications [21]. Crosslinking a melt of precursor chains leads to a polymer network with a complex, quenched, random connectivity and topology [22], which macroscopically behaves as a (viscoelastic) solid. Computer simulations allow the full, microscopic characterization of a polymer network, for example in the form of the Kirchoff matrix characterizing the network connectivity [15,23], and sequences of topological invariants such as the Gauss linking number characterizing the topological state [12,24–26]. The question is, whether this vast amount of (experimentally inaccessible) detailed microscopic information is really needed. From a physical view point, one would expect that the properties of polymer networks should be

---

* Corresponding author. Tel.: +49 3518711210; fax: +49 3518711999.
E-mail address: zqex@mpipks-dresden.mpg.de (C. Svaneborg).

0032-3861/$ - see front matter © 2005 Elsevier Ltd. All rights reserved.
doi:10.1016/j.polymer.2005.03.008

self-averaging, i.e. that they depend on the averaged characteristics of the many possible realizations of quenched connectivity and topology. While the calculation of suitable averages over the quenched disorder is far from trivial, theories of rubber elasticity [1,16–20] derive the macroscopic elastic response from a description of the average localization and deformation of parts of the network as a function of a small number of physically motivated parameters such as the density of chemical cross-links and entanglements.

In the present paper we use MD simulations to investigate how the central quantities of rubber elasticity theory are affected by disorder in the microscopic connectivity of polymer networks. For this purpose we compare randomly crosslinked and randomly end-linked model polymer networks with nearly identical average strand lengths. Both types of systems have been used experimentally to test theories of rubber elasticity [27–35] and their respective advantages have been a matter of debate. As in Ref. [36] we present our results within the framework of the double tube model [37], because it provides quantitative relations between microcopic and macroscopic observables.

The structure of this paper is as follows. In the next section we present a brief introduction to tube models models for polymer networks with emphasis on the double tube model. In Section 3, the polymer model, simulation methodology, and crosslinking procedure are described. In Section 4 characterization of the resulting networks is presented. The analysis of the simulation data in terms of the tube model are presented in Section 5 and our conclusions are presented in Section 6.

2. Theory

A polymer melt or network is a challenging many-body statistical mechanics problem. Chains have random walk configurations, and since they can not pass through each other, a single chain is entangled with many other chains. Entanglement constraints transiently restrict the conformation space available for thermal fluctuations, and cause the chain to become localized. When a melt is crosslinked chemical bonds are added between monomers, causing the chain to be localized even further. The resulting network is characterized by a quenched connectivity. During the process of crosslinking the topological state of the network is also quenched. The tube concept proposed by Edwards [38] provides a tractable simplification of the statistical mechanics of polymer melts and networks. The idea is to model the complex many body-effects by a single effective harmonic confining potential, that represents the collective localization effects experienced by a single chain due to its neighborhood [22].

Tube models [19,39–43] derives their name from the possible chain conformations, which occupy a fuzzy tube-shaped region of space. By superposing many conformations of a network strand the tube progressively becomes visible [45,46]. See Figs. 3 and 4. The tube is characterized by single parameter d_T denoting the tube diameter or equivalently the Kuhn length of the tube axis (the so-called ‘primitive-path’ [47]). The tube diameter is a length scale that depends not only on the instantaneous state of the network, but also on the precursor melt state and the process by which it was crosslinked. No formal derivation has so far succeeded in deriving the tube model directly from first principles, since the introduction of topological constraints into statistical mechanical theories has proven to be very complex, see e.g. [48–52]. Recently, it has become possible to extract the tube diameter directly from simple topological analysis of the primitive-path mesh-work of simulated model polymer melts and networks [53]. While the tube diameter with its strain dependence is a central quantity in in tube theories, it is not directly experimentally observable. It is regarded as a phenomenological parameter, either fitted or inferred from other observables such as the plateau modulus measured in rheological experiments [27,28,33,34] or the structure factor obtained from scattering experiments [54,55].

The confinement due to crosslinks and entanglements are qualitatively different. An entanglement is free to slip along the chain contours, while crosslinks are fixed chemical bonds. Hence, it is not surprising that a qualitatively different behavior is observed in the limits where only crosslink or entanglement confinement exists. The phantom model [56–59] captures the effects due to the network connectivity. However, it completely neglects entanglements. Constrained junction models [60–63] derive their name from the attempt of introducing the effects of entanglements by constraining the fluctuation of network junctions.

Tube models stress the importance of constraining the fluctuations of the entire network strand. Using replica techniques [39] Deam and Edwards [22,64] showed that the localization due to crosslinks can be represented as an effective strain independent confinement potential. This tube model is denoted model A in the following. Just as the phantom model predicts isotropic and strain-independent fluctuations of crosslinkers, model A predicts an isotropic and strain-independent tube diameter $d_{T,A}(\lambda_\alpha) = d_{T,A}$. Here λ_α denotes the strain in the α’th Cartesian direction.

Gaylord and Douglas [43,44] modelled the combined effect of connectivity and entanglement confinement. By assuming an affine deformation of junction points, Cartesian separability of the tube, and a constant volume of the deforming tubes, their model predicted $d_T(\lambda_\alpha) = d_T/\sqrt{\lambda_\alpha}$.

Heinrich and Straube [19] and later Rubinstein and Panyukov [65] also modeled the effect of entanglement confinement. They used an affinely transforming confining potential, e.g. one where the strain dependence of the confinement spring constant is $l(\lambda_\alpha) = l(1)\lambda_\alpha^{-2}$. Their tube model is refered to as model B in the following, and it predicts an anisotropic strain-dependent tube diameter $d_{\mathrm{T,B}}(\lambda_\alpha)=\sqrt{\lambda_\alpha d_{\mathrm{T,B}}}$.

A scaling argument relates the strain dependence of the confinement springs to the tube diameters. For a random walk, after n steps the displacement is $d^2\sim b^2 n\sim k_{\mathrm{B}}Tn/k$ where the step length is b, or equivalently k is the strength of the connectivity springs. The energy increase due to the confinement potential is $\sim ld^2$ per step. The average displacement given by the total energy $\sqrt{kl}d^2\sim K_{\mathrm{b}}T$. Since the right hand side and the connective springs are strain independent, $d^2(\lambda_\alpha)\sim 1/\sqrt{kl(\lambda_\alpha)}$.

In general, a Cartesian component of the tube diameter can be a function of the full strain tensor $\Lambda_{\alpha\beta}$, i.e. $d_{\mathrm{T},\alpha}(\Lambda_{\alpha\beta})$. In the following, we will assume that different Cartesian components α of vectorial network observables, such as the tube diameter, are independent. This is tantamount to assuming that the statistical distribution characterizing the network state can be factorized into a product of each of the three Cartesian directions. We denote the α'th component of the strain dependent tube diameter $d_{\mathrm{T}}(\lambda_\alpha)$, since the extra Cartesian subscript for $d_{\mathrm{T},\alpha}$ is superfluous. This fails when, e.g. finite-extensibility effects are important [1] or if the network has been crosslinked from an anisotropic melt state. In order to simplify the notation, quantities stated without explicit strain dependence are to be evaluated for the unstrained network, e.g. $d_{\mathrm{T,B}}\equiv d_{\mathrm{T,B}}(\lambda_\alpha=1)$.

The double tube model [37] derives its name from the fact that it use two correlated and additive confining potentials to represent the combined effects due to crosslinks and entanglements. While the confining potentials are assumed to be additive, the expressions for microscopic deformations and stress–strain relations display a complicated non-linear dependence on the relative strength of the two confining potentials. The double tube model gives an effective anisotropic and strain-dependent tube diameter based on the two components by the addition relation [37].

$$\frac{1}{d_{\mathrm{T}}^4(\lambda_\alpha)}=\frac{1}{d_{\mathrm{T,A}}^4}+\frac{1}{\lambda_\alpha^2 d_{\mathrm{T,B}}^4} \tag{1}$$

The purpose of a theory of rubber elasticity is to link the microscopic conformational response to an imposed macroscopic strain to the resulting macroscopic stress. The microscopic strain response is modelled by the strain-dependence of the confining potential, or equivalently the strain-dependence of the tube diameter, as in Eq. (1). For a Gaussian theory such as the double tube model the microscopic conformations are completely characterized by the mean-square distances

$$r_\alpha^2(|i-j|,\lambda_\alpha)=\langle[r_{\alpha,i}(t;\lambda_\alpha)-r_{\alpha,j}(t;\lambda_\alpha)]^2\rangle \tag{2}$$

where i and j denotes beads on a network strand or in an extended path through part of the network. The average is not only over time but also over network strands or realizations of paths through the network. $r_{i,\alpha}(t;\lambda_\alpha)$ denotes the α'th Cartesian component of the position of the i'th bead at time t in a network under strain λ_α. The unstrained mean-square distances are abbreviated $r_\alpha^2(n)$. In the following we will also assume that the strand statistics of the unstrained network and the precursor melt is the same and Gaussian, i.e. that the unstrained mean-square distance is given by $r_\alpha^2(n)=b^2n$, where b is the statistical segment length of one Cartesian component. The microscopic response to strain is completely characterized by the dimensionless ratio

$$f=\frac{r_\alpha^2(n,\lambda_\alpha)-r_\alpha^2(n)}{\lambda_\alpha^2 r_\alpha^2(n)-r_\alpha^2(n)} \tag{3}$$

At large length scales rubber is a solid, and hence it deforms in an affine manner (i.e. $f=1$). However, due to the inextensible nature of chemical bonds affine deformation can not persist down to monomeric length scales, where the chains are in a liquid-like state. The extension of bonds between monomers are unaffected by the deformation ($f=0$), however, their average orientation will be affected by the strain. The length scale defining the crossover between these two very different deformation regimes is the tube diameter. On a scaling level, the degree of affinity f is expected to be a universal function of the scaling parameter $y=r_\alpha^2(n)/[2d_{\mathrm{T}}^2(\lambda_\alpha)]$. The double tube model predicts

$$f(y)=f_{\mathrm{A}}(y)+\frac{d_{\mathrm{T,A}}^4}{d_{\mathrm{T,A}}^4+\lambda_\alpha^2 d_{\mathrm{T,B}}^4}[f_{\mathrm{B}}(y)-f_{\mathrm{A}}(y)] \tag{4}$$

where $f_{\mathrm{A}}(y)=1+(\exp(-y)-1)/y$ and $f_{\mathrm{B}}(y)=1+0.5\exp(-y)+1.5(\exp(1-y)-1)/y$ are two different scaling functions describing confinement due to crosslinks and entanglements respectively.

The normal tension $\sigma_{\mathrm{T}}(\lambda)=\sigma_\parallel-\sigma_\perp$ can be deduced by regarding the network as being made up of ideal independent Gaussian strand segments [66] of length n. The density of segments is $\rho_{\mathrm{s}}(n)=\rho/n$ where ρ is the monomeric density. Each segment is regarded as an entropic spring with spring constant $k_{\mathrm{B}}T/r_\alpha^2(n)$, where $r_\alpha^2(n)$ is the mean-square distance for a precursor chain. The mean end-to-end extension in parallel and perpendicular directions is denoted by $r_\parallel^2(n,\lambda_\parallel)$ and $r_\perp^2(n,\lambda_\perp)$. Hence, the Gaussian segmental normal tension derived from the virial tensor can be expressed using only mean-square distances as

$$\sigma_{\mathrm{T}}(n,\lambda)=k_{\mathrm{B}}T\rho_{\mathrm{s}}(n)\left[\frac{r_\parallel^2(n,\lambda_\parallel)}{r_\alpha^2(n)}-\frac{r_\perp^2(n,\lambda_\perp)}{r_\alpha^2(n)}\right] \tag{5}$$

Historically, there has been some debate on how to choose the segment length scale n at which the 'Gaussian' normal tension should match the macroscopic normal tension. A natural choice (made by all classical theories of rubber elasticity [1,56–63]) is to set n equal to the average strand length. Tube models calculate normal tensions from the limit n toward 0. Combining Eqs. (3)–(5) and taking the limit, the double tube model makes the following prediction for the stress–strain relation

$$\sigma_T(\lambda) = (\lambda_\parallel^2 - 1)g(\lambda_\parallel) - (\lambda_\perp^2 - 1)g(\lambda_\perp) \tag{6}$$

$$g(\lambda_\alpha) = \frac{\rho k_B T}{8} \frac{b^2}{d_T^2(\lambda_\alpha)} \frac{d_{T,A}^4 + 2\lambda_\alpha^2 d_{T,B}^4}{d_{T,A}^4 + \lambda_\alpha^2 d_{T,B}^4} \tag{7}$$

The crosslink dominated limit is given by $d_{T,A} \ll d_{T,B}$, i.e. where crosslinks cause the strongest confinement. In this limit $g \propto b^2/d_T^2$ becomes strain independent, and the classical stress–strain is $\sigma_T(\lambda) \propto \lambda^2 - \lambda^{-1}$ regained. A more complicated stress–strain behavior is observed in general. Our prior simulation results show that the double tube model can successfully describe the microscopic deformations in the crossover from networks dominated by entanglement to crosslink confinement [36]. Based on fitting the microscopic deformations to estimate the unstrained crosslinked and entanglement tubes, the double tube model was furthermore seen to make accurate predictions for the stress–strain relation when compared to the simulation results.

3. Simulation methodology

The networks were simulated using the molecular dynamics method which has been successfully applied to study entanglement effects in polymer melts [67,68]. In this model the polymers are represented as freely jointed bead-spring chains. All monomeric units of mass m interact via a purely repulsive Lennard–Jones potential

$$U_{LJ}(r) = \begin{cases} 4\varepsilon\left[\left(\frac{\sigma}{r}\right)^{12} - \left(\frac{\sigma}{r}\right)^6 + \frac{1}{4}\right] & \text{for } r < r_c \\ 0 & \text{for } r \geq r_c \end{cases} \tag{8}$$

where $r_c = 2^{1/6}\sigma$. This choice is similar to a hard-core potential but allows simulation by standard molecular dynamics methods. Monomer units connected along the chain or through the crosslinking procedure are connected by a finite extensible non-linear elastic (FENE) potential

$$U_{FENE}(r) = \begin{cases} \frac{-R_0^2 k}{2} \ln\left[1 - \left(\frac{r}{R_0}\right)^2\right] & \text{for } r < R_0 \\ \infty & \text{for } r \geq R_0 \end{cases} \tag{9}$$

The model parameters are the same as in Ref. [67]. The temperature is $T = \varepsilon/k_B$, and the basic unit of time $\tau = \sigma(m/\varepsilon)^{1/2}$. The simulations are carried out at a constant monomeric density $\rho = 0.85\sigma^{-3}$. The equations of motion were integrated using the velocity-Verlet algorithm where all monomers are weakly coupled to a Langevin heat bath with coupling $\Gamma = 0.5\tau^{-1}$ [45,67]. We used a time step of $\Delta t = 0.012\tau$ and all simulations were performed using the LAMMPS code [69]. Most of the simulations were run on 36 processors of Sandia's ICC Intel Xeon cluster. The statistical segment length for one Cartesian component of the equilibrated chains is $b = 0.7528\sigma$ [70]. One of the most important features of this model is that the energy barrier for the crossing of two chain segments is high enough ($\approx 70 k_B T$) such that crossing is virtually impossible.

We studied both randomly crosslinked and end-linked networks. In all cases we started from equilibrated melts M×N [70] specified in Table 1. Here M denotes the number of chains, and N the chain length. For the randomly crosslinked networks, a monomer is chosen at random and all neighboring monomers within a reaction radius $r_x = 1.3\sigma$ are identified. A new bond is then added between the randomly chosen monomer and one of its neighbors chosen at random provided the two monomers are either on different chains or at least a chemical distance of three monomers apart if on the same chain. To investigate the effects of self-loops and dangling ends we ran some variations of the crosslinking procedure to avoid these defects. To eliminate self-loops networks ($C100_2$) were also made in which the minimum chemical distance along the same chain was increased to 300. The procedure was then repeated until the specified number of bonds was added. To produce random networks without dangling ends ($C100_3$), all 2 M end monomers are first attached to a neighboring monomer at random before the remaining crosslinks are added. All the extra crosslinks for these random networks are added instantaneously. For the end-linked networks, one quarter of the chain ends are chosen at random and attached to a $f = 4$-functional crosslinker. When a free end comes within the reaction radius r_x of an unsaturated crosslinker, the free end is connected to all the other ends which are already attached to the crosslinker. The crosslinking procedure was run until the defect free fraction of the network exceeded 91%. For more details see Ref. [45].

The elastic modulus and non-linear stress versus strain are easily measured experimentally for networks. Numerically the shear modulus is obtained from uniaxial, volume conserving elongation of the sample described by a diagonal strain tensor $\Lambda = \Delta(\lambda_x, \lambda_y, \lambda_z)$ with the stretching factor $\lambda_x = \lambda$ in the parallel direction and the contraction factors $\lambda_y = \lambda_z = \lambda^{-1/2}$ in perpendicular directions.

The normal stress σ_T is then readily determined from the microscopic virial tensor $\sigma_T = \sigma_{xx} - (\sigma_{yy} + \sigma_{zz})/2$, where x is the direction of elongation. Here the deviatoric part of the virial tensor is defined as $\sigma_{\alpha\beta} = V^{-1}\langle \sum r_{ij,\alpha} F_{ij,\beta} \rangle$ where the sum is over unique pairs i and j of interacting beads, r_{ij} the separation between beads. F_{ij} is force either due to the FENE springs or the LJ excluded volume interactions. In the present simulations we vary λ from 4.0 (extension) to 0.6 (compression). Due to finite system size, we are limited to relatively large strains $\lambda > 1.2$ or $\lambda < 0.8$. For smaller strains, the stress is small and difficult to determine accurately from the noise. After an initial step strain, the strain decays very slowly. For the longest mean strand length studied ($N_s = 100$), runs typically of at

Table 1
Networks

Network	Description
E100	2500 × 100 end-linked network
$C100_1$	80 × 3500 melt with 1400 random cross links
$C100_2$	80 × 3500 melt with 1400 random cross links, with no self-loops
$C100_3$	80 × 3500 melt with 1400 random cross links, with no dangling ends
C100	Average of observables sampled using $C100_1$, $C100_2$, $C100_3$
E20	5000 × 20 end-linked network
C20	80 × 3500 melt with 7000 random cross links

least $10^5\tau$ ($5\times10^4\tau$ for $N_s=20$) were needed to reach equilibrium.

4. Characterization of networks

After the crosslinking procedure is complete, we characterize the network in terms of average strand length, average croslink functionality and network defects. Uncrosslinked chains, dangling ends, and self-loops are defects, which are identified by a burning algorithm that repeatedly identifies and removes the defects until the defect free network is identified. Network defects can still be elastically active, because they relax slowly compared to the duration of a simulation. Due to this we have not attempted to correct the sampled stresses to take account of the defect free fraction of the network.

Characterizations of all the networks studied are presented in Table 2. For all the networks, the fraction of beads in the defect free fraction is above 90%. The fraction of strands in the defect free fraction is above 85%, i.e. these are strands where both ends are connected. For the randomly crosslinked networks roughly 10% of all the strands form closed self-loops, except for $C100_2$ where the crosslinking procedure was modified to inhibit the formation of self-loops. Dangling ends constitute less than 6% of all the strands. The crosslinking procedure for $C100_3$ prevented dangling ends. The defect free part of the network has a approximately 10% larger strand length, and a somewhat smaller average functionality. This is due to the removal of the predominantly short self-loops. The gel fraction is larger than 99.6% for all the networks.

The strand length distribution is shown in Fig. 1. End-linked networks are monodisperse by construction. For randomly crosslinked networks we observe as expected an exponential $P(n)=\langle n\rangle^{-1}\exp(-n/\langle n\rangle)$ [71]. For this distribution 63% of the strands will have less than the average length, but they only contain 26% of the beads. 6% of the strands will be longer than $3\langle n\rangle$, and they contain 20% of all beads.

Note, that it is important to distinguish between effects due to network defects and connective disorder. Since we can identify the defect parts of the network structure, we can discard these, and focus on observing the effects that are caused by disorder.

5. Analysis

We are interested in how network heterogeneities due to connective disorder affect network observables. Of particular interest for rubber elasticity theory is confinement which gives rise to localization, the network strain response which gives rise to microscopic deformations, and the macroscopic stress–strain relation. It is the goal of any theory of rubber elasticity to predict the macroscopic stress from the microscopic deformations response to an imposed strain.

5.1. Visualization

Fig. 2 shows the localization of three segments. The same three chain segments are shown for both the strongly (C20) and weakly ($C100_3$) crosslinked networks. Because both the strongly and weakly networks have been crosslinked from the same precursor melt state, the three segments appears very similar. To visualise how the strands are connected to

Table 2
Network characterizations

	d.f. beads	d.f. strands	Self-loops	$\langle n\rangle$ w.d.	$\langle n\rangle$ wo.d.	$\langle f\rangle$ w.d.	$\langle f\rangle$ wo. d.
E100	0.92	0.92	0.02	100.0	100.0	3.9	3.7
$C100_1$	0.91	0.85	0.09	100.9	108.6	4.1	3.6
$C100_2$	0.94	0.94	0.00	100.4	100.8	4.1	4.0
$C100_3$	0.97	0.90	0.10	106.1	115.4	4.0	3.6
E20	0.94	0.94	0.04	20.0	20.0	4.0	3.8
C20	0.95	0.90	0.09	23.2	24.3	4.4	4.0

Defect free fraction of network beads, defect free fraction of network strands, self-loop fraction of strands, average strand length with and without defects, and average crosslink functionality with and without defects.

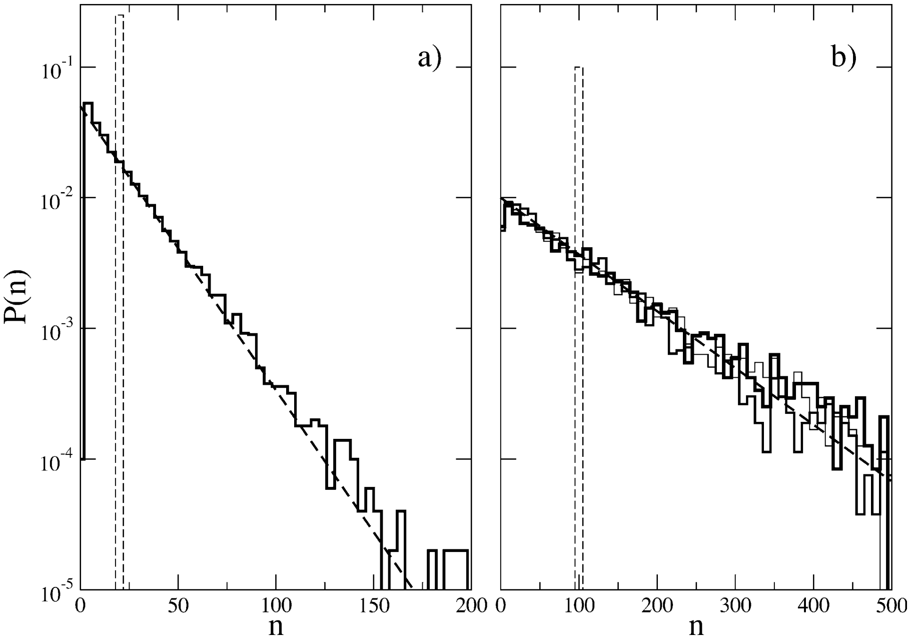

Fig. 1. Strand length distribution of the defect free part of the network (a) E20 (thin dashed) C20 (solid) (b) E100 (thin dashed), $C100_1$, $C100_2$, $C100_3$ (solid lines with increasing thickness). The thick dashed line is $P(n)$ with $\langle n\rangle = 20$ and 100, respectively.

the rest of the network, the beads on the pendant chains have been shown up to a chemical distance of 20 beads away from the three segments. The segment length is 500 beads, corresponding to either an average of 25 or five crosslinks along the segment, which explains the 'hairy' appearance of the strongly crosslinked network. Due to the exponential strand length distribution crosslinks are very unevenly distributed along the segments, which is especially clear from the weakly crosslinked network.

Figs. 3 and 4 show the tube localization of three segments shown in Fig. 2. The cloud of points consists of the superposition of all bead positions in the sampled trajectory [45], and show the range of excursions available for thermal fluctuations subject to cross-link and entanglement constraints. A single strand configuration is also shown. The length of the simulation trajectories is $120k\tau$ and $58k\tau$, for the weakly and strongly randomly crosslinked networks, respectively, which is much larger than the entanglement time $\tau_e \sim 1100\tau$ that was estimated by Pütz et al. [72].

When networks are strained, the microscopic conformations respond by being deformed. While it is difficult to compare the large scale structural change between the strained and unstrained conformations, the local structure appear to be very similar as expected. To visualise the large scale strain dependence of the microscopic deformations, we transform the strained segment conformations back into the unstrained box, where they are compared directly to the unstrained state. The back transform is made by an inverse affined scaling transformation $r_{i,\alpha}(\lambda_\alpha) \rightarrow r_{i,\alpha}(\lambda_\alpha)/\lambda_\alpha$ which leaves an affinely deforming bead $r_{i,\alpha}(\lambda_\alpha) = \lambda_\alpha r_{i,\alpha}$ invariant. A sub-affine or strain-independent deformation response will appear as compressed along the x direction and

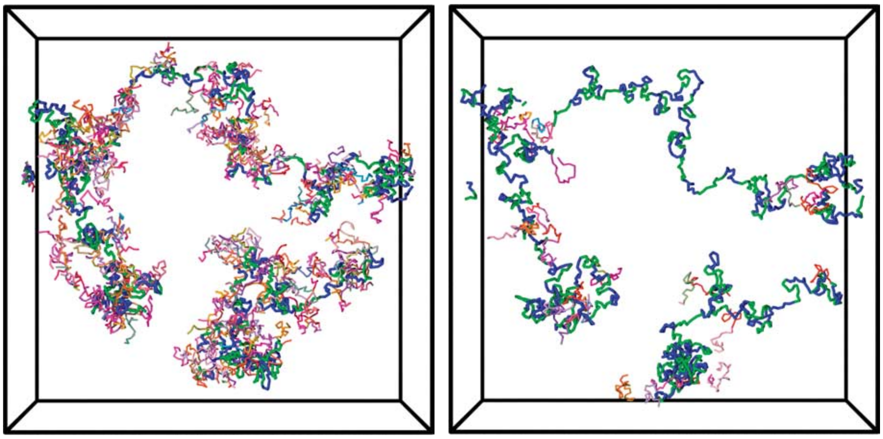

Fig. 2. Visualization of three segments (thick blue/green) and their pendant chains (thin red) for C20 (left) and $C100_3$ (right) for $\lambda = 1$ (see text for details).

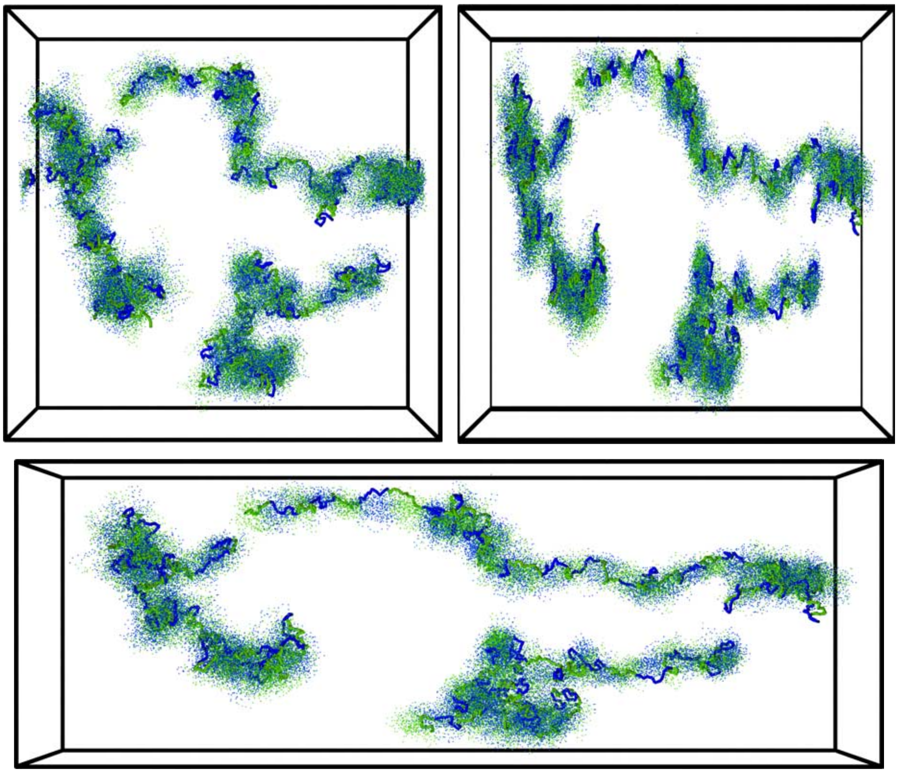

Fig. 3. Visualization of tube localization for C20 for $\lambda=1$ (top left), $\lambda=2$ affinely back transformed into the unstrained box (top right), and $\lambda=2$ (bottom) (for details see the text).

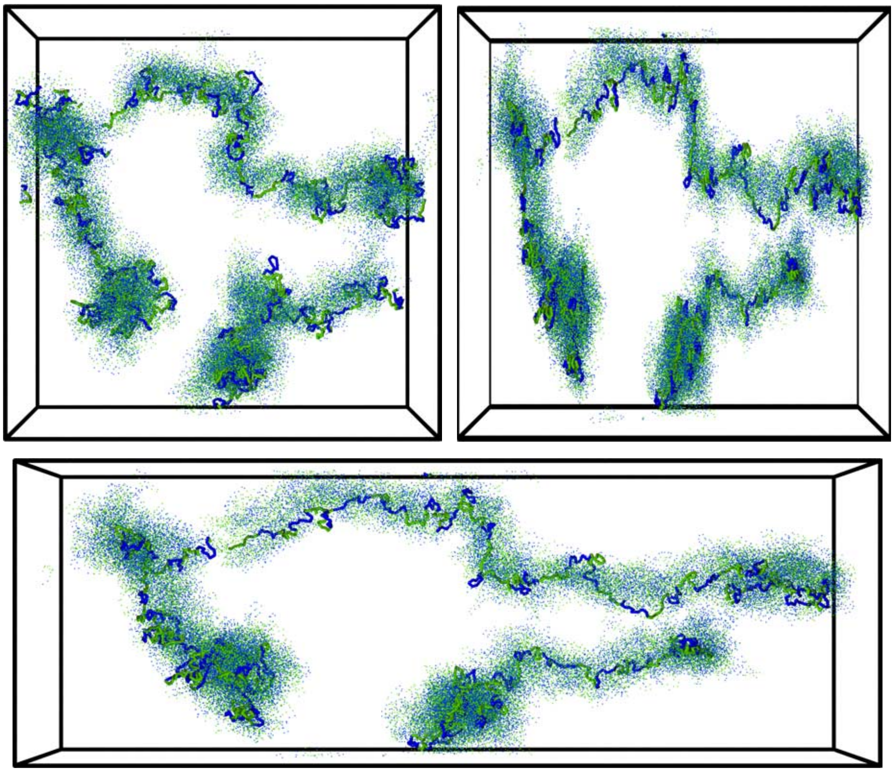

Fig. 4. Visualization of tube localization for $C100_3$, for $\lambda=1$ (top left), $\lambda=2$ affinely back-transformed into the unstrained box (top right), and $\lambda=2$ (bottom).

stretched in the *yz* plane (shown as the thickness of the frame of the box). Comparing the unstrained and back transformed strained conformations shows that the large scale structure remains invariant, i.e. the position of the tube deforms affinely. At short length scales, however, the segments appears to be affected by the back-transform indicating sub-affine strain dependence.

The tube diameters are given by the width of the cloud parallel and perpendicular to the strain direction. Comparing the strongly crosslinked (Fig. 3) and weakly crosslinked (4) networks shows that increasing the number of crosslinks leads to stronger localization, and hence a decrease of the tube diameter, a similar behavior is observed for the strained networks. It is difficult to discern any strain dependence of the tube diameter for the strongly crosslinked networks, however, the tube diameter for the weakly crosslinked network shows sub-affine strain dependence.

Entanglements only localize transverse fluctuations with respect to the local tube axis, while crosslinks localize both longitudinal and transverse fluctuations. To visualize the effects of longitudinal fluctuations, the segments were divided into blocks of 10 beads each, which are shown with an alternating blue and green color. For the weakly crosslinked network (Fig. 4) the cloud appears to be an uniform mixture of the two colors, indicating that longitudinal fluctuations smears the colors along the tube contour. For the strongly crosslinked networks (Fig. 3) the cloud can at places be observed to be alternating between the blue and green. This shows that increasing the number of crosslinks atleast partially freeze the longitudinal fluctuations. Note that seven blocks corresponds to one entanglement length N_e, which appears roughly to match the step length of the tube.

5.2. Path ensembles

In order to quantitatively probe effects of network heterogeneities, we need to sample observables not only averaged over the entire network, but also for suitably chosen sub-components. For this purpose, we have generated a set of path ensembles. The strand length of the precursor chains for the randomly crosslinked networks is 3500 beads. On each precursor chain, we identified 30 segments of length 100. When the precursor melt is crosslinked, these segments becomes extended paths that traverse through part of the network structure. Paths containing network defects were removed. Furthermore, only the middle part of each precursor chain was used to avoid effects due to the dangling ends. The paths were sorted into bins depending on the number of crosslinks that then traversed. The ensemble of paths traversing m crosslinks will be denoted P_m. The number of paths in each P_m is shown in Table 3. Besides taking averages over all beads in a path, it is interesting to take averages restricted to the crosslinks in each path ensemble. This ensemble of crosslinker beads is denoted X_m.

Table 3
Number of paths in the P_m ensembles for the randomly crosslinked networks

	$C100_1$	$C100_2$	$C100_3$	C20
P_0	957	898	1024	31
P_1	704	840	749	96
P_2	312	447	282	197
P_3	102	138	88	240
P_4	24	40	25	210
P_5				232
P_6				179
P_7				121
P_8				74
P_9				41

5.3. Localization

In order to characterize localization, we sample the mean-square displacements defined as

$$g_{1,\alpha}(t) = \langle [r_{i,\alpha}(t) - r_{i,\alpha}(0)]^2 \rangle \tag{10}$$

The average is taken not only over time but also an ensemble of beads, for instance all crosslinks, all beads, or one of the path ensembles. At short time scales the mean-square displacement shows a diffusive behavior, while at large time scales the mean-square displacement reaches a plateau that characterises the spatial localization. We define the fluctuation radius as $u_\alpha^2 = g_{1,\alpha}(t \to \infty)/2$. The extrapolation is done by performing a least-squares fit of $g(u^2\zeta) = 2u^2[1 - \exp(-\sqrt{t/[u^4\zeta]})]$ to the sampled $g_{1,\alpha}(t)$, where ζ denotes a strain-dependent friction parameter.

The fluctuation radii sampled for a number of different ensembles are shown in Fig. 5. The same qualitative behavior is observed with regard to strain-dependence for strongly and weakly crosslinked networks, however, stronger localization is observed for the stronger crosslinked network.

Fig. 5(a) and (b) shows the fluctuation radii averaged over paths in the P_m ensembles. Paths in the P_0 ensemble do not traverse crosslinks, as a result they only experience the constraints due to entanglements with neighboring chains. Segments on such a path have full freedom to perform curvilinear, longitudinal fluctuations along the tube in which they are confined. We observe $u_\alpha^2(\lambda_\alpha) \sim \lambda_\alpha$ a strain response, corresponding to the expectation of the strain-dependence of the entanglement tube [19,65].

The longitudinal fluctuations gradually become suppressed for path ensembles traversing more crosslinks. This is observed to cause a gradual decrease of the fluctuation radii, and a much weaker strain response. This is expected from the Warner–Edwards tube model [64] which accounts only for the confinement due to crosslinks. The model predicts strain independent fluctuations. Fig. 5(c) and (d) shows the fluctuation radii sampled for the X_m crosslink ensembles. Compared to the P_m ensembles, the restriction to only averaging over crosslinks is observed to cause the

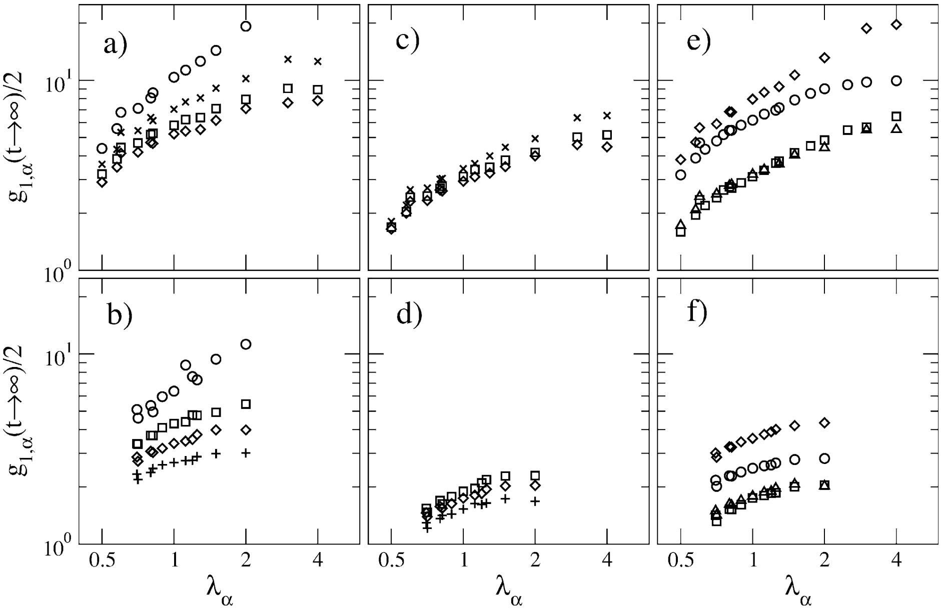

Fig. 5. Strain-dependent localization averaged over different ensembles. Networks with average strand length 100 (top row) and 20 (bottom row). Localization averaged over P_m paths (left column), X_m crosslinks (center column), and for all beads or crosslinks (right column). Symbols are as follows: (a) C100 sampled using P_0 (○), P_1 (x), P_2 (□), P_3 (◇) (b) C20 sampled using P_0 (○), P_2 (□), P_4 (◇), P_8 (+) (c) C100 sampled using X_1 (x), X_2 (□), X_3 (◇) (d) C20 sampled using X_2 (□), X_4 (◇), X_8 (+) (e) E100 sampled using all beads (○), C100 sampled using all beads (◇), E100 sampled using all crosslinks (□), C100 sampled using all crosslinks (△) (f) E20 sampled using all beads (○), C20 sampled using all beads (◇), E20 sampled using all crosslinks (□), C20 sampled using all crosslinks (△).

fluctuation radii to display a very weak dependence on the number of crosslinks traversed as well as a rather weak strain dependence.

A clear difference is observed when comparing the fluctuation radii for all beads in the end-linked and randomly crosslinked networks, shown in Fig. 5(e) and (f). The reason is the network heterogeneity, where the longitudinal fluctuations of segments on long strands make a large contribution to the fluctuation radii for the randomly crosslinked networks compared to end-linked networks. The fluctuation radii averaged over all crosslinks, however, are not affected.

5.4. Microscopic deformations

Fig. 6 shows the microscopic deformations obtained by averaging mean-square distances $r^2_\alpha(\lambda_\alpha, n)$ over the ensembles used in Fig. 5(a). The microscopic deformations follow the behavior expected from the theory, i.e. they show a crossover from a strain-independent behavior at short distances to affine (i.e. $r^2_\alpha(\lambda_\alpha, n)/r^2_\alpha(n) = \lambda^2_\alpha$) behavior at large distances. For path ensembles with an increasing number of crosslinks, the location of the crossover shifts slightly, indicating a change of the tube diameter.

To obtain the tube diameters, the double tube model was fit to the microscopic deformations analyzing all the sampled strains as well as the parallel and perpendicular components simultaneously. Logarithmically distributed data points were used to reduce the large number of correlated data points at large n. At large distances the deformation is affine, and the microscopic deformations does not contain any information about the tube diameter. The two unstrained tube diameters, $d_{T,A}$ and $d_{T,B}$, were fit simultaneously, the effective strain dependent tube diameter d_T is then given by Eq. (1) and the prediction for the microscopic deformations by Eqs. (3) and (4). The statistical error was estimated by a block analysis over 10 subsets of paths.

The resulting tube diameters for the P_0, P_2, and P_4 ensembles are shown in the insert of Fig. 6. Compared to the fluctuation radii shown in Fig. 5(a), the corresponding tube diameters are observed to be only weakly affected by which path ensemble is used, in particular the strain-dependence is not affected.

To characterize the deformation response averaged over the entire network, we have sampled mean-square distances along paths of length 500 through the networks. For randomly crosslinked networks, we used all the defect free paths that were generated for studying network heterogeneities. We generated random non-reversible paths through the defect free part of the end-linked networks, to have a comparable path ensemble. In all cases, the path length was five times the average strand length of the networks.

The same behavior of the microscopic deformations averaged over the entire network is observed for the end-linked and randomly crosslinked networks shown in Fig. 7(a) and (b). The slight horizontal shift indicates a slight increase of the tube diameter for the randomly crosslinked networks. The three different variations of the random

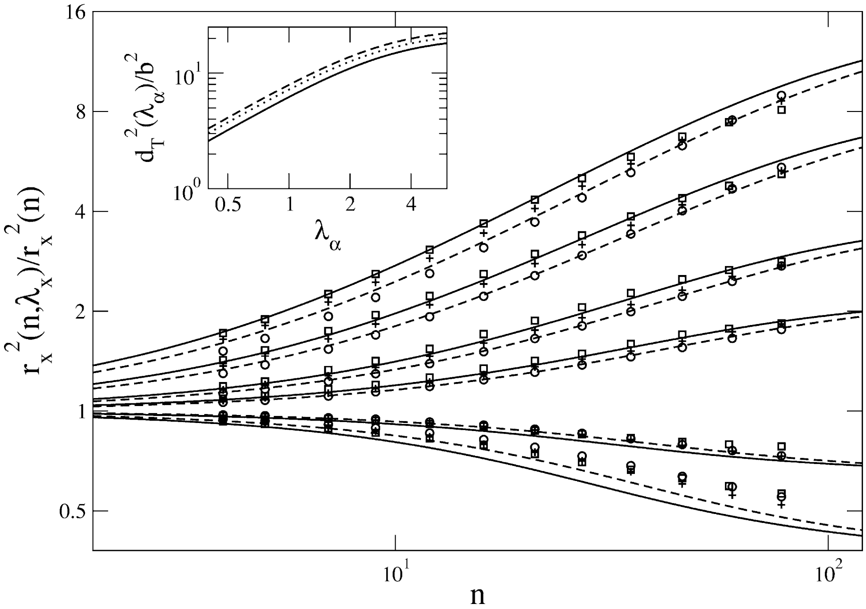

Fig. 6. Parallel component of microscopic deformations sampled for P_0 (○), P_2 (+), P_4 (□), for $\lambda = 0.6, 0.8, 1.5, 2, 3, 4$ for C100. Lines are fit of the double tube model to P_0 (dashed) and P_4 (solid). The insert shows the strain dependence of the fitted tube diameter for P_0 (dashed), P_2 (dotted), and P_4 (solid).

crosslinking (Fig. 7(c)) are observed not to have any discernible effect.

The double tube model is seen to provide an accurate description of the microscopic deformations, not only for the ideal end-linked networks, but also for the randomly crosslinked networks. The results for the fits are summarized in Table 4. The strongly and weakly randomly crosslinked networks are observed to have a 14% and 7% larger tube diameter, respectively, compared to the end-linked networks. A deviation between the theory and sampled microscopic deformations is observed for the weakly crosslinked systems at large strains and small n in the perpendicular direction. This deviation causes a systematic error of the fit parameters. We fitted the data restricted to $y \in [0.1{:}1]$ and $y \in [1{:}10]$ separately, to estimate the error of our fit parameters due to this effect. We observe that the systematic error is about a factor of two larger than the statistical error.

The entanglement tube diameter $d_{T,B}$ is systematically smaller than the crosslink tube diameter $d_{T,A}$ for all the

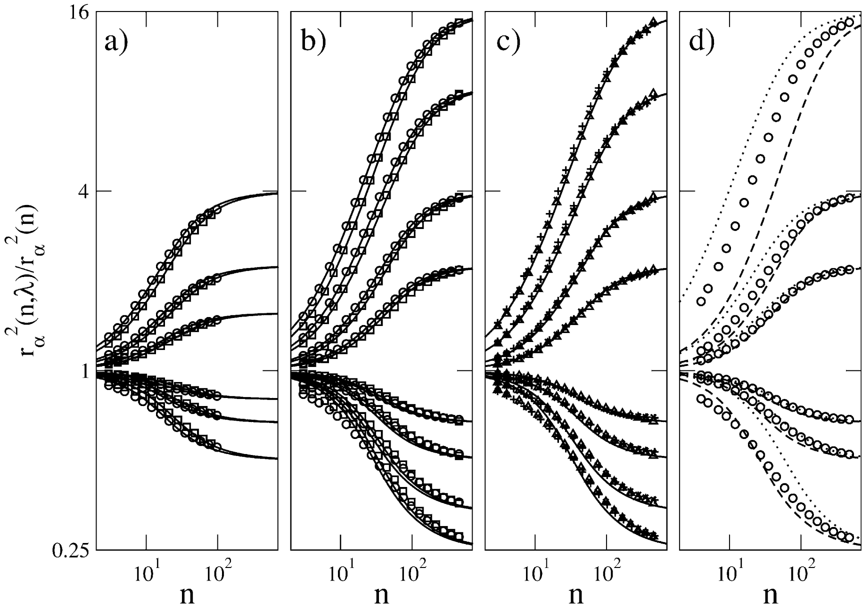

Fig. 7. Parallel and perpendicular microscopic deformations (a) E20 (○) and C20 (□) for $\lambda = 1.25, 1.5, 2$ (b) E100 (○) and $C100_1$ (□) for $\lambda = 1.5, 2, 3, 4$ (c) $C100_1$ (△), $C100_2$ (+), $C100_3$ (x) for $\lambda = 1.5, 2, 3, 4$ (d) E100 (○) for $\lambda = 1.5, 2, 4$. Lines are fits of the double tube model (solid), pure crosslink confinement (dotted), pure entanglement confinement (hashed).

Table 4
Fit results

System	Data points	d_T/b	$d_{T,a}/b$	$d_{T,b}/b$	χ^2_{red}
E100	342	2.57 [2.47,2.70]	4.54 [4.05,5.13]	2.63 [2.46,2.73]	32.56
$C100_1$	216	2.77 [2.56,3.12]	5.10 [4.07,7.12]	2.84 [2.59,3.07]	5.89
$C100_2$	216	2.74 [2.51,3.12]	4.85 [4.09,5.84]	2.82 [2.55,3.32]	5.04
$C100_3$	216	2.80 [2.56,3.17]	4.83 [4.00,6.45]	2.88 [2.59,3.39]	4.14
C100		2.77 [2.53,3.03]	5.01 [4.05,6.14]	2.76 [2.55,3.13]	
E20	120	1.94 [1.80,2.14]	2.67 [2.31,3.09]	2.11 [1.87,2.75]	3.28
C20	180	2.21 [1.96,2.53]	3.05 [2.61,3.95]	2.39 [2.01,3.68]	1.69

Values in brackets denotes the systematic error.

networks. This indicates that both networks are in a regime where entanglement confinement is the strongest localization effect. It is surprising that the strongly crosslinked system with average strand length 20 is still dominated by entanglements when the entanglement length is $N_e = 70$. The limit of weak crosslinking/long strands obviously corresponds to a melt, however, our results suggest a complex interplay of connectivity and topology is present in the limit of strong crosslinking, which behaves very differently than expected from the phantom model limit $d_{T,A} \ll d_{T,B}$ of the double tube model.

The double tube model consists of two components representing crosslink and entanglement confinement potentials, respectively. It is natural to ask if both components are really required to represent the simulation data. By fixing either $d_{T,B}$ or $d_{T,A}$ at a large value, the double tube model reduces to the Warner–Edwards tube model (model A) or the Heinrich–Straube/Rubinstein–Panyukov entanglement tube model (model B) respectively. Fig. 7(d) shows the fits to these two limiting cases for the E100 network. Clearly, neither of the two components are able to provide an accurate description of the microscopic deformations at strains larger than $\lambda \sim 2$, whereas the double tube model is very good agreement with the data for all strains. This shows that while entanglements are the strongest source of localization compared to crosslinks, neither confinement effect can alone provide a good description of the microscopic deformations. Similar results has been found for other networks studied.

5.5. Macroscopic stresses

The question is at which segment size is the normal tensions expected to match the macroscopic normal tensions. Since both the sampled microscopic deformations and the theoretical predicted deformations are available for our simulated networks on all length scales, this question can be addressed directly.

The sampled values for the length scale dependent normal tensions Eq. (5) are plotted in Fig. 8. A natural choice made by all classical theories of rubber elasticity [1,56–63] is to set n equal to the average strand length, which is shown to systematically underestimate the macroscopic normal tension. Fig. 8 indicates that relevant deformations occur down to scales on the order of the tube diameter, below which $\sigma_T(n,\lambda)$ becomes independent of n. Thus the limit n toward 0, in which the normal tensions are calculated in the tube model, is not critical in the present case. However, this would not be the case for a network made of semi-flexible chains.

Fig. 9 shows the stress–strain relations obtained directly by sampling the microscopic virial tensor, the 'Gaussian' normal tensions, and the prediction based the double tube model fits to the microscopic deformations. The stress–strain relation for the end-linked and randomly crosslinked networks are observed to be very similar, except for a decrease in the shear modulus for the randomly crosslinked networks. This is directly related to the corresponding increase of the tube diameter for this networks. Good agreement is also observed between the simulation results (10% error bar) and the stress–strain relation predicted by the double tube model (estimated to have a 30% error bar).

The 'Gaussian' normal tensions evaluated at the average strand length is about a factor of two off compared to the normal tensions obtained by sampling the microscopic virial tensor. However, the 'Gaussian' normal tensions extrapolated to n toward 0 is observed to be in perfect agreement with the predicted stress–strain relation, and in good agreement with the virial normal tensions. We have previously observed that the 'Gaussian' normal tensions constitute approximately 90% of the normal tension obtained using the microscopic virial tensor [36].

Clearly, estimating the macroscopic stresses from a mesoscopic model representing the network as ideal Gaussian chain segments is a subtle point, as it has been discussed by Gao and Weiner [73]. Furthermore, when the crosslinking process is not instantaneous the statistics of the unstrained network can differ from that of the precursor melt. If the crosslinking process causes network strands to be stretched relative to the precursor melt, then the normal tensions will be underestimated. It is worth noting that better agreement would be observed if we had fit the theoretical stress–strain relation directly to the sampled stresses, however, the goal of a theory for rubber elasticity is to relate microscopic deformations and macroscopic stresses, and predicting the macroscopic stresses based on the sampled microscopic deformations provides a much more stringent test of the microscopic assumptions on which theories are based.

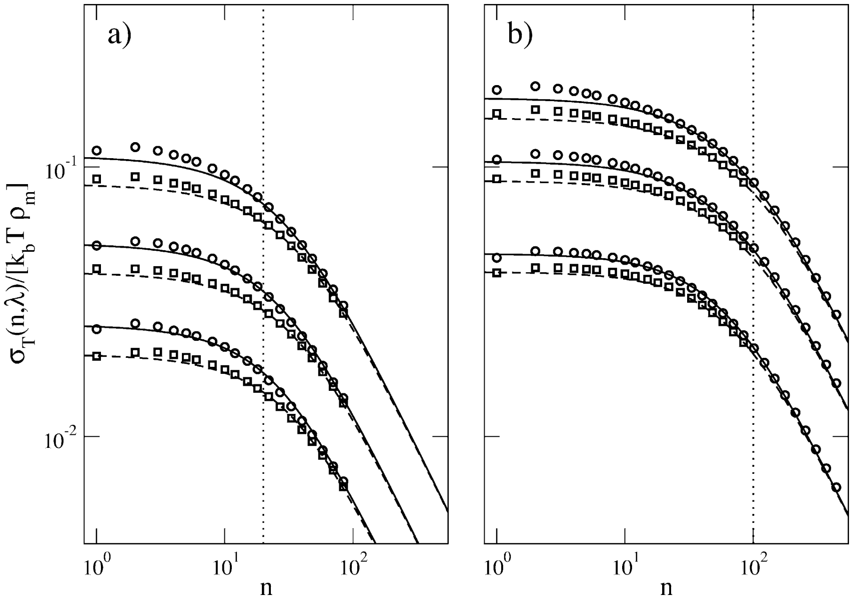

Fig. 8. Length scale dependent normal tensions Eq. (5) expressed using sampled mean-square distances (symbols) and the double tube model Eqs. (3) and (4) (solid and dashed line) (a) E20 (○) and C20 (□) for $\lambda = 1.25, 1.5, 2$ (b) E100 (○) and C100 (□) for $\lambda = 2, 3, 4$. The average strand length is illustrated by a dotted line.

6. Conclusions

We have end-linked and randomly crosslinked equilibrated polymer melts to produce two comparable sets of model networks characterized by the same average strand length but very different strand length distributions. This connective disorder causes randomly crosslinked networks to be more heterogeneous compared to end-linked networks. We have investigated the effects of network heterogeneities on the observables relevant for rubber elasticity theories, i.e. localization, microscopic deformation response to macroscopic strain, and the macroscopic stress–strain relation.

For all observables, the averages over the entire network show negligible differences between randomly crosslinked and end-linked networks. One exception is the fluctuation radii averaged over all beads, which is directly related to the large contribution from the longitudinal fluctuations of segments on long strands in the randomly crosslinked networks. Nonetheless, more detailed analysis show effects due to heterogeneity in the networks. These effects are much

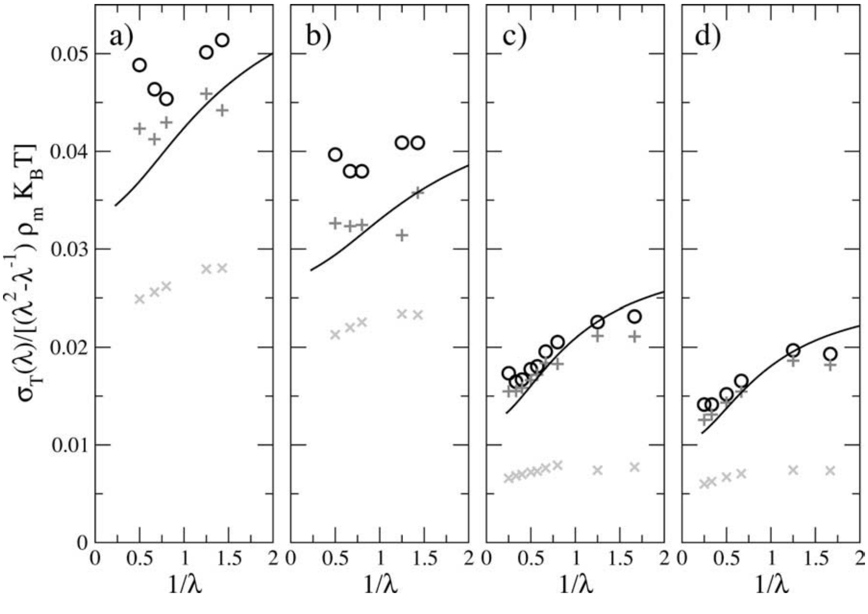

Fig. 9. Mooney–Rivlin plot of stress–strain relations (a) E20 (b) C20 (c) E100 and (d) C100. Symbols are as follows: normal tension from microscopic virial tensor (○), extrapolated 'Gaussian' normal tension (+), 'Gaussian' normal tension evaluated at the average strand length (x). The solid line is the double tube theory prediction.

more pronounced for the localization compared to the microscopic deformations of the networks, which are only weakly affected by disorder and longitudinal fluctuations.

Our results show that the double tube model can describe the microscopic deformations not only for the case for the highly idealized end-linked networks, but that it is also applicable to more realistic randomly crosslinked networks. The double tube model, furthermore, provide predictions for the macroscopic stresses, which are in good agreement with the sampled stress–strain relation. We observe that both the tube diameter and the stress–strain relation are rather insensitive to the network heterogeneities.

In future work, we will investigate how the scattering functions are affected by network heterogeneities, and using the procedure presented in Ref. [53] we can characterize not only the connected state of the network, but also directly investigate the primitive path meshwork and its strain dependence, which should provide an explanation of why the randomly crosslinked networks are observed to have a larger tube diameter, and why the entanglement confinement still dominate for the strongly crosslinked system. We will also compare how swelling affects the network heterogeneities for random and end-linked networks.

Acknowledgements

Sandia is a multiprogram laboratory operated by Sandia Corporation, a Lockheed Martin Company, for the United States Department of Energy's National Nuclear Security Administration under contract DE-AC04-94AL85000.

References

[1] Treloar LRG. The physics of rubber elasticity. Oxford: Clarendon; 1975.
[2] Erman B, Mark J. Annu Rev Phys Chem 1989;40:351.
[3] Dünweg B, Grest GS, Kremer K. In: Binder K, editor. Numerical methods for polymeric systems. New York: Springer-Verlag; 1998. p. 159.
[4] Kremer K, Grest GS. In: Binder K, editor. Monte Carlo and molecular dynamics simulations in polymer science. New York: Oxford University Press; 1995. p. 194.
[5] Heine DR, Grest GS, Lorenz CD, Tsige M, Stevens MJ. Macromolecules 2004;37:3857.
[6] Kindt JT. J Phys Chem B 2002;106:8223.
[7] Gilra N, Cohen C, Panagiotopoulos AZ. J Chem Phys 2000;112:6910.
[8] Gilra N, Panagiotopoulos AZ, Cohen C. J Chem Phys 2001;115:1100.
[9] Sharaf M, Kloczkowski A, Mark J. Comput Theor Polym Sci 2001;11:251.
[10] Sharaf M, Mark J. Polymer 2002;43:643.
[11] Tsige M, Lorenz C, Stevens MJ. Macromolecules 2004;37:8466.
[12] Michalke W, Lang M, Kreitmeier S, Göritz D. J Chem Phys 2002;117:6300.
[13] Bhawe DM, Cohen C, Escobedo FA. Macromolecules 2004;37:3924.
[14] Lay S, Sommer J-U, Blumen A. J Chem Phys 1999;110:12173.
[15] Sommer J-U, Lay S. Macromolecules 2002;35:9832.
[16] Doi M, Edwards SF. The theory of polymer dynamics. Oxford: Clarendon; 1986.
[17] Mark JE, Erman B. Elastomeric polymer networks. Englewood Cliffs, NJ: Prentice Hall; 1992.
[18] Rubinstein M, Panyukov S. Macromolecules 2002;35:6670.
[19] Heinrich G, Straube E, Helmis G. Adv Polym Sci 1988;85:33.
[20] Kloczkowski A. Polymer 2002;43:1503.
[21] Mark J. Prog Polym Sci 2003;28:1205.
[22] Deam RT, Edwards SF. Philos Trans R Soc London A 1976;280:317.
[23] Shy L, Eichinger B. J Chem Phys 1989;90:5179.
[24] Everaers R, Kremer K. Phys Rev E 1996;53:R37.
[25] Michalke W, Lang M, Kreitmeier S, Göritz D. Phys Rev E 2001;64:012801.
[26] Lang M, Michalke W, Kreitmeier S. J Compos Phys 2003;185:549.
[27] Higgs PG, Gaylord RJ. Polymer 1990;31:70.
[28] Gottlieb M, Gaylord RJ. Polymer 1983;24:1644.
[29] Gottlieb M, Gaylord RJ. Macromolecules 1984;17:2024.
[30] Gottlieb M, Gaylord RJ. Macromolecules 1987;20:130.
[31] Meissner B. Polymer 2000;41:7827.
[32] Patel SK, Malone S, Cohen C, Gillmor JR, Colby RH. Macromolecules 1992;25:5241.
[33] Urayama K, Kawamura T, Kohijya S. J Chem Phys 1996;105:4833.
[34] Urayama K, Kawamura T, Kohijya S. Macromolecules 2001;34:8261.
[35] Hild G. Prog Polym Sci 1998;23:1019.
[36] Svaneborg C, Grest GS, Everaers R. Phys Rev Lett 2004;93:257801.
[37] Mergell B, Everaers R. Macromolecules 2001;34:5675.
[38] Edwards SF. Proc Phys Soc 1967;92:9.
[39] Edwards SF, Vilgis TA. Rep Prog Phys 1988;51:243.
[40] McLeish TCB. Adv Phys 2002;5:1379.
[41] Marrucci G. Macromolecules 1981;14:434.
[42] Gaylord RJ. J Polym Bull 1982;8:325.
[43] Gaylord R, Douglas J. J Polym Bull 1987;18:347.
[44] Gaylord R, Douglas J. J Polym Bull 1990;23:529.
[45] Duering ER, Kremer K, Grest GS. J Chem Phys 1994;101:8169.
[46] Edwards SF. Proc R Soc London A 1988;419:221.
[47] Edwards SF. Br Polym J 1977;9:140.
[48] Edwards SF. Proc Phys Soc 1967;91:513.
[49] Edwards SF. J Phys A 1968;1:15.
[50] Kholodenko A, Vilgis T. Phys Rep 1998;298:251.
[51] Kleinert J. Path integrals in quantum mechanics, statistics and polymer physics. Singapore: World Scientific; 1995.
[52] Ferrari F, Lazzizzera I. Nucl Phys B 1999;559:673.
[53] Everaers R, Sukumaran S, Grest G, Svaneborg C, Sivasubramanian A, Kremer K. Science 2004;303:823.
[54] Westermann S, Urban V, Pyckhout-Hintzen W, Richter D, Straube E. Macromolecules 1996;29:6165.
[55] Straube E, Urban V, Pyckhout-Hintzen W, Richter D, Glinka CJ. Phys Rev Lett 1995;74:4464.
[56] James H. J Chem Phys 1947;15:651.
[57] Flory PJ. Proc R Soc London Ser A 1976;351:351.
[58] James HM, Guth E. J Chem Phys 1947;11:455.
[59] Higgs PG, Ball RC. J Phys (France) 1988;49:1785.
[60] Ronca G, Allegra G. J Chem Phys 1975;63:4990.
[61] Flory PJ. J Chem Phys 1977;66:5720.
[62] Erman B, Flory PJ. J Chem Phys 1978;68:5363.
[63] Kästner S. Colloid Polym Sci 1981;259.
[64] Warner M, Edwards SF. J Phys A 1978;11:1649.
[65] Rubinstein M, Panyukov S. Macromolecules 1997;30:8036.
[66] Gao J, Weiner JH. Macromolecules 1987;20:2525.
[67] Kremer K, Grest GS. J Chem Phys 1990;92:5057.
[68] Pütz M. Dynamik von Polymerschmelzen und Quellverhalten ungeordneter Netzwerke. PhD Thesis, University of Mainz; 1999.
[69] Plimpton S. J Compos Phys 1995;117:1.
[70] Auhl R, Everaers R, Grest GS, Kremer K, Plimpton SJ. J Chem Phys 2003;119:12718.
[71] Grest GS, Kremer K. Macromolecules 1990;23:4994.
[72] Pütz M, Kremer K, Grest GS. Europhys Lett 2000;49:735.
[73] Gao J, Weiner JH. Science 1994;266:748.